

Nanophotonic near-field levitated optomechanics

Lorenzo Magrini,¹ Richard A. Norte,² Ralf Riedinger,¹ Igor Marinković,² David Grass,¹
Uroš Delić,¹ Simon Gröblacher,^{2,*} Sungkun Hong,^{1,†} and Markus Aspelmeyer^{1,‡}

¹*Vienna Center for Quantum Science and Technology (VCQ),*

Faculty of Physics, University of Vienna, A-1090 Vienna, Austria

²*Kavli Institute of Nanoscience, Delft University of Technology, 2628CJ Delft, The Netherlands*

Optical control of trapped dielectric objects provides a remarkably simple, yet versatile platform for studying a plethora of intriguing problems in single molecule biophysics [1, 2], thermodynamics [3–6], sensing [7, 8] or fundamental physics [9, 10]. Realizing full quantum control of trapped nanoparticles will enable new insights into quantum-enhanced precision metrology as well as into fundamental aspects of quantum physics [11, 12]. One of the major challenges is to efficiently transduce and manipulate the particle motion at the quantum level. Here we present a nanophotonic platform suited to solve this problem. By optically trapping a 150 nm dielectric particle in the vicinity of the near field of a photonic crystal cavity, at a distance of ~ 310 nm from its surface, we achieve strong, tunable single-photon optomechanical coupling of up to $g_0/2\pi = 9$ kHz, three orders of magnitude larger than previously reported for levitated cavity optomechanical systems [13, 14]. In addition, efficient collection and guiding of light through our nanophotonic structure results in a per-photon displacement sensitivity that is increased by two orders of magnitude when compared to state-of-the-art far-field detection [15]. The demonstrated performance shows a promising route for quantum optical control of levitated nanoparticles.

The past few years have witnessed rapid progress towards the quantum regime of optically levitated nanoparticles through cavity- [13, 14, 16, 17] and feedback-assisted control schemes [15, 18–20]. The primary limitations lie either in small optomechanical coupling strengths to the cavity field, or, for the case of optical tweezers, in significant losses in the detection channel. As every scattered photon induces back-action noise on the particle motion, it is crucial not to ‘lose’ any information carried by light [21], especially in the regime where photon recoil is the dominant source of decoherence. Nanophotonic structures can provide a solution to these problems. Their small mode volumes and high quality factors result in strong optomechanical coupling [22, 23]. These nanostructures can also be easily interfaced with a single mode fiber, hence allowing for efficient collection and guiding of the light from the cavity [24]. Previously, optical nanodevices have been used, for example, to show strong coupling and super-radiance of trapped atoms [25, 26], emission rate control of solid state quantum emitters [27, 28], label-free single molecule detection [29], or backaction induced dynamics of colloidal particles in liquid [30].

Here we use a nanophotonic cavity to efficiently couple the mechanical displacements of a levitated nanoparticle to a single optical mode. By placing the particle at a distance of ~ 310 nm from a photonic crystal cavity, and exploiting the dispersive coupling to the evanescent component of the strongly confined cavity field, information about the mechanical displacement is encoded into phase fluctuations of the cavity mode [22]. This signal can be guided through fibers to a detector, ideally with near unity efficiency, enabling quantum

optomechanical control of both cavity field and particle motion [31].

Our experimental setup consists of an optical tweezer and a silicon nitride (SiN) photonic crystal cavity (Fig. 1a), both of which are situated inside a vacuum chamber. The cavity is impedance matched, with a fundamental resonance wavelength of $\lambda_{cav} = 1538.72$ nm and an optical loss rate of $\kappa/2\pi = 5.0$ GHz. The input/output mirror is adiabatically transitioned into a tapered waveguide that is interfaced with an open-end tapered fiber [24], yielding a fiber-to-cavity coupling efficiency of $\eta_{cav} = 0.32$. Taking into account all other losses in the setup, the total detection efficiency of photons approaching the cavity is $\eta = 0.09$ (see SI). The fiber physically supports the nanocavity by van der Waals forces and can be positioned relative to the optical tweezer using a piezo-actuated three-axis translational stage. The optical tweezer is formed by tightly focusing the laser beam (wavelength $\lambda_{trap} = 1064$ nm; trap power 150 mW) with a commercial dry objective lens (numerical aperture $NA = 0.95$) inside the vacuum chamber. The location of the trap within the focal plane is controlled by steering the angle of incidence of the laser at the rear lens of the objective.

Ultimately, the particle is trapped in a standing wave potential formed by the interference of the focused trapping light with its reflection off the surface of the photonic crystal. To achieve this we first trap a neutral silica nanoparticle (nominal radius $r = 71.5 \pm 2.0$ nm) with the optical tweezer at ambient pressure [40]. After reducing the pressure to 1.5 mbar, we bring the nanocavity in close proximity to the particle. During this process, the optical trap potential is transformed adiabatically from the single, nominally Gaussian, potential given by the focal spot of the tweezer, to the periodic potential induced by the standing wave [25] (Fig. 1a). The locations and actual shapes of the multiple lattice sites are determined by the wavelength of the trap beam and the thick-

* s.groebblacher@tudelft.nl

† sungkun.hong@univie.ac.at

‡ markus.aspelmeyer@univie.ac.at

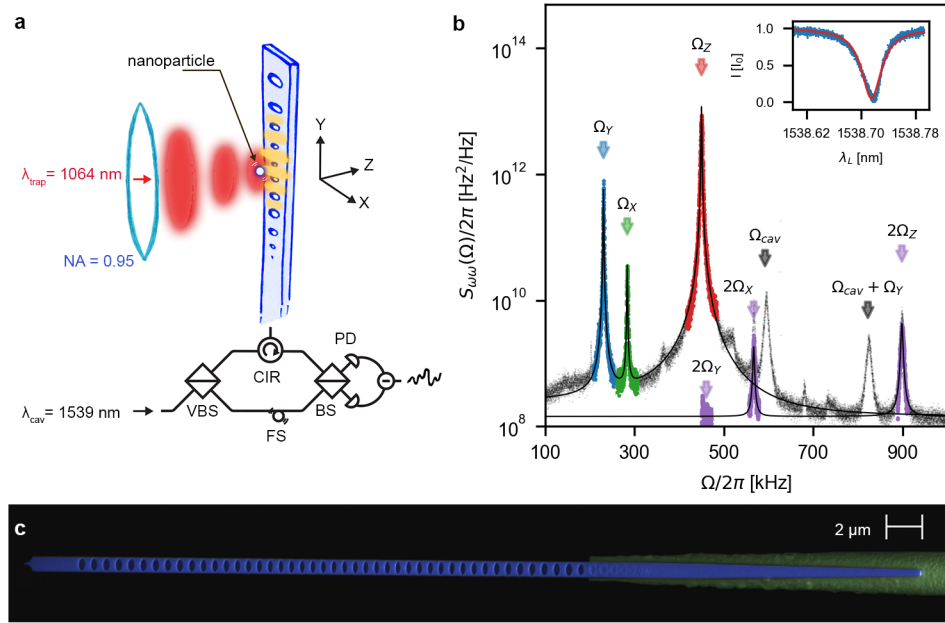


FIG. 1: Nanophotonic interface. **a**, Sketch of the setup: A dielectric nanoparticle is trapped inside the high intensity lobe formed by the reflection of the optical tweezer light ($\lambda_{trap} = 1064$ nm) from the surface of the nanophotonic cavity, at a distance of about 310 nm. A laser light on resonance with the cavity ($\lambda_{cav} = 1538.72$ nm) is sent into a variable beam splitter (VBS) which splits it into a weak (260 nW) beam pumping the cavity, and a strong (1 mW) local oscillator. The cavity output is redirected by a circulator (CIR) towards a symmetric beam splitter (BS) at which it interferes with the local oscillator. The light in the two output ports is measured using a balanced photo-detector (PD). While the low frequency component of the signal is used to stabilize the interferometer via a fiber stretcher (FS), the high frequency part is directed to a signal analyzer. **b**, The measured frequency power spectral density exhibits three mechanical peaks at $\Omega_y/2\pi = 228.3$ kHz (blue), $\Omega_x/2\pi = 280.3$ kHz (green) and $\Omega_z/2\pi = 444.9$ kHz (red). The significantly higher frequency along z , which is the direction of the tweezer beam propagation, is caused by the standing wave confinement, and for the radial directions x and y , the degeneracy is broken due to the use of polarized light together with tight focusing. Nonlinearities in the trap potential as well as in the optomechanical couplings result in peaks at twice the mechanical frequencies (highlighted in purple). The mechanical vibration of the cavity/fiber assembly at around the frequency $\Omega_{CAV}/2\pi \sim 600$ kHz also induces additional peaks in the spectrum. The inset shows the cavity resonance measured by monitoring the light reflection from the cavity while scanning the pump laser wavelength. The slight asymmetry of the response arises from thermo-optic effects, as we are pumping the cavity at the limit of thermal stability (see SI). **c**, False-colored SEM image of the photonic crystal cavity (blue) attached to the tapered fiber (green).

ness of the cavity (see SI and [25, 32]). Our experimental parameters yield the first minimum of the trapping potential at $z_0 \sim 380$ nm from the device surface, i.e. a surface-to-surface separation between nanosphere and photonic crystal cavity of $d = z_0 - r \sim 310$ nm. Due to the subwavelength transverse dimensions of the nanophotonic device, the cavity field exhibits a considerable evanescent component that decays exponentially with distance. In this region, the displacement of the particle results in a shift of the cavity resonance by $\delta\omega_{cav} = G_\xi \delta\xi$, where $\xi = x, y, z$ is the direction of mechanical motion and $G_\xi = \partial_\xi \omega_{cav} \propto \partial_\xi E^* E$ the optomechanical coupling (E : evanescent field amplitude). As G_ξ is proportional to the intensity gradient of the cavity field along the direction of motion, each mechanical mode couples to the cavity field with different strength. In particular, the small mode volume results in a large field variation and hence a significantly enlarged coupling when compared to standard levitated optomechanics configurations based on bulk optics [13, 14, 16].

When pumping the cavity on resonance, the position dependent frequency fluctuation is mapped onto the phase quadra-

ture of the output field, which can then be measured via a shot-noise limited homodyne detection (Fig. 1a). We use this cavity-enhanced measurement to monitor the thermal motion of the trapped particle: the mechanical oscillations in the three spatial directions are observed as distinct frequency components in the homodyne signal (Fig. 1b). Using thermal noise of the particle motion and photon shot noise of the cavity light we calibrate both displacement and optomechanical coupling (see SI). We note that, by only injecting 260 nW of optical power into the cavity and at an overall detection efficiency of 9%, we achieve a displacement sensitivity of $(3.3 \pm 0.5) \times 10^{-12}$ m/ $\sqrt{\text{Hz}}$, similar to what is measured in far field detection with 1 mW of detected light. This amounts to an increase in the position sensitivity per-photon by more than a factor of 100. At the optimal position we measure coupling rates along the z -direction of motion, i.e. orthogonal to the cavity surface, of $G_z/2\pi = 3.6 \pm 0.4$ MHz/nm. This is in good agreement with our finite element (FEM) simulation and corresponds to a single-photon optomechanical coupling $g_0/2\pi \equiv G_z/2\pi \cdot z_{ZPF}$ of 9.3 ± 0.9 kHz ($z_{ZPF} = \sqrt{\hbar/2m\Omega_z}$:

mechanical zero point fluctuation of the particle motion in the z direction).

Another intriguing feature of photonic crystal cavities is the strong spatial variation of the cavity field E , which results in a significant position-dependent optomechanical coupling for all three spatial directions of motion. By changing the particle position relative to the cavity we can therefore tune the optomechanical coupling of all mechanical modes [33]. We experimentally demonstrate this by scanning the particle position in a plane perpendicular to the z axis while simultaneously monitoring the cavity signal. The observed strong modulations in all three coupling rates are in good agreement with FEM simulations (Fig. 2). As the levitated nanoparticle represents

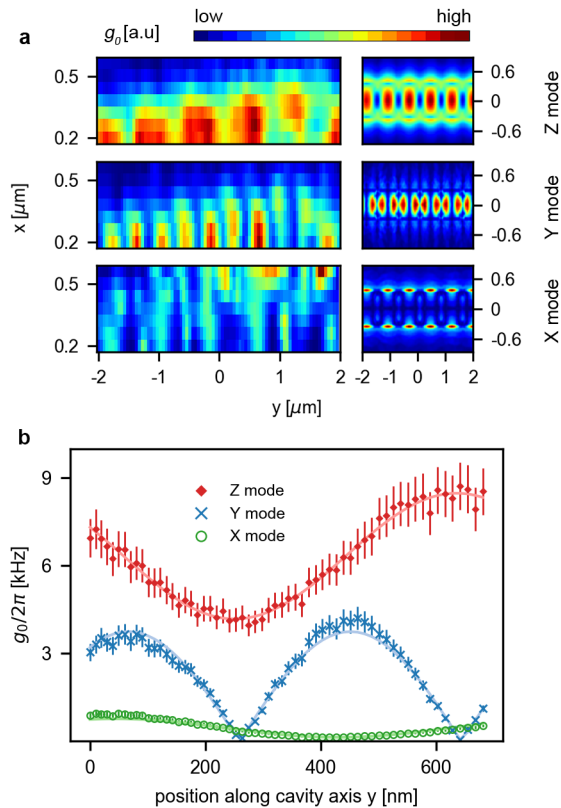


FIG. 2: **Optomechanical coupling.** **a**, Measured (left) and simulated (right) intensity map of the single photon optomechanical coupling rates g_0 for the three spatial modes. Because of heating from the tweezer light (see SI), at every position the cavity is reset on resonance before recording the interferometric signal. A Gaussian filter of $\sigma = 1$ pixel is applied to the maps in order to reduce noise arising from inaccuracy in coarse positioning. The tilt in the measured maps is due to slow position drifts of the clamped fiber supporting the photonic crystal. **b**, Position scan of the optomechanical coupling rates along the y direction and close to the cavity center for the modes along x (green circles), y (blue crosses) and z (red diamonds). Solid lines are fits based on our cavity field model (see SI). As the scan was performed slightly off the cavity center, the coupling to the z mode is non-vanishing while we can suppress the x and y couplings. The main contribution to the error bars is given by the uncertainty in the shot noise level determined by the integration time of ~ 3 seconds.

a sub-wavelength probe, this measurement allows us to image the three dimensional intensity gradient of the nanophotonic cavity mode in super-resolution, i.e. not limited by diffraction (Fig. 2). Compared to previous mappings using atoms [25] our high optomechanical coupling allows for a much faster acquisition (seconds versus hours of acquisition time per data point).

Our system also enables tunability of the mechanical frequencies without affecting the coupling strength to the cavity field. In other words, we can modify the trapping potential independent of the trapping distance. To demonstrate this we move the cavity along the z direction, away from the focus of the trapping beam (Fig. 3a). The optomechanical coupling stays constant (Fig. 3c), indicating that the relative distance between the particle and the cavity remains unchanged. This behavior can easily be understood when considering the formation of the standing wave by the cavity reflection. The positions of the anti-nodes are solely determined by the location of the cavity and its thickness, locking the trap position to the cavity. At the same time, the mechanical frequency is reduced because the high divergence of the tightly focused optical tweezer leads to a sharp decrease of the intensity at the trap location (Fig. 3b,d).

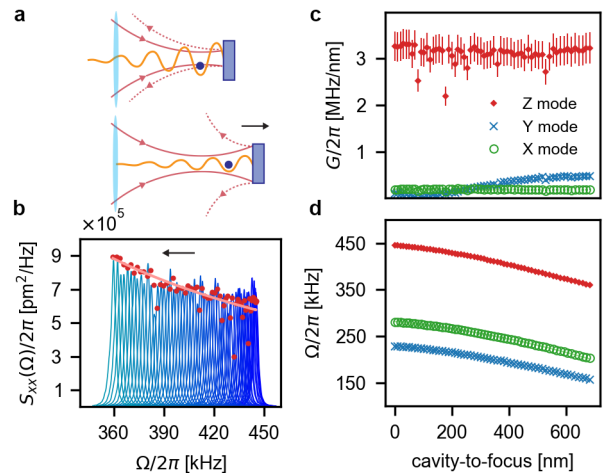


FIG. 3: **Position locking.** **a**, Sketch of the nanoparticle (blue dot), trapped in the standing wave potential (orange) formed by the reflection of the focused tweezer light (red) by the photonic crystal cavity (grey rectangle). The data is taken by moving the photonic crystal along the direction of propagation of the tweezer beam (z). While the particle's distance to the cavity remains locked, the divergence of the tweezer causes a reduction of the trapping potential. **b**, Position power spectral density for the z mode $S_{zz}(\Omega)$ (blue) measured as cavity-focus increases (in direction of the arrow). The variance of the motion given by the peak integral (red dots $\propto \int S_{zz}(\Omega)d\Omega$) changes with the mechanical frequency as stated by the equipartition theorem (pink solid line $\propto 1/\Omega_z^2$). Deviation from the expected Lorentzian peak is given by the fluctuations during the integration time, which effectively reduce the peak height. **c**, Frequency shift per displacement G plotted as a function of the cavity distance to the focal plane, for the z mode (red diamonds), y mode (blue crosses) and x mode (green circles). **d**, Mechanical frequencies for the three modes as a function of the cavity distance to the focal plane.

Finally, we demonstrate reliable, deterministic loading of the nanoparticle into the different standing wave optical lattice sites. This is achieved by a sequence of optical tweezer and cavity position control steps (Fig. 4a). We first terminate the standing wave by moving the particle to the side of the photonic crystal cavity. After displacing the cavity along the z axis, the particle is moved back and the standing wave reestablished. When the cavity is sufficiently displaced, the particle will slide into the next trap location of the re-appearing standing wave. We observe this behavior when the cavity displacement is greater than $\lambda_{trap}/4$ (Fig. 4c). At this second trap location, the optomechanical coupling rate is reduced by two orders of magnitude, consistent with FEM simulation (see Fig. 4b and SI).

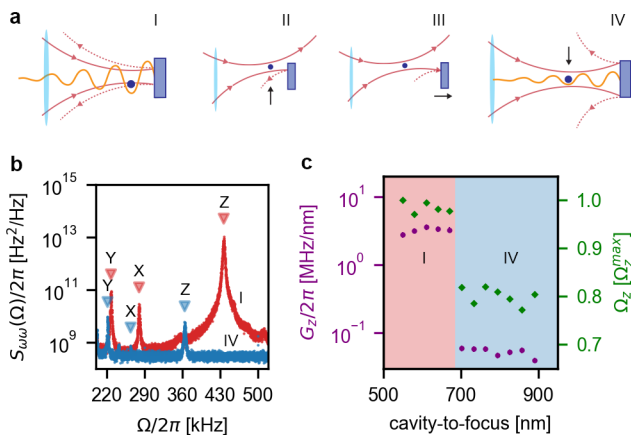


FIG. 4: **Loading of the particle into the lattice.** **a**, The particle is initially trapped in the closest of the cavity trap sites (I). We steer the tweezer away from the cavity (II) and subsequently change the cavity position (III). Finally the particle is steered back in front of the cavity (IV). Depending on the cavity-to-focus distance, the particle will slide into different sites. **b**, Frequency power spectral densities measured in the case of the particle being in the first trapping site (red, I) or in the second (blue, IV). The small unlabeled peak in the blue spectrum is a noise peak common to all measurements. **c**, Optomechanical coupling (purple dots) and mechanical frequency (green diamonds) for the z mode as a function of the initial cavity-to-focus distance.

In summary, we have realized a low-loss, and widely tunable hybrid optomechanical system combining optical levitation of a nanoparticle with a nanophotonic cavity via near-field coupling. The detection efficiency of our platform is more than two orders of magnitude higher than what was shown using far-field detection [15]. It is thereby already approaching the value of $\eta = 1/9$ required for ground-state feedback cooling [34, 35]. We anticipate that an improved alignment procedure will increase the fiber-to-cavity coupling efficiencies to values exceeding 96%, as was previously shown by Burek *et al.* [24], which will yield overall detection efficiencies beyond 30%.

An important figure of merit for quantum state control is the quantum cooperativity $C_q = (4g_0^2 n_{cav})/(\kappa \gamma_m n_{th})$, where n_{cav} (n_{th}) and κ (γ_m) are the optical cavity photon (mechanical phonon) number and loss rate [31]. With the cur-

rent experimental parameters $C_q \sim 10^{-9} \ll 1$, which is far from the system's full potential, but can be improved beyond $C_q > 1$ rather straightforwardly. Currently, the main bottleneck is the mechanical support of the cavity, which causes alignment drifts and hence limits feedback particle stabilization in (ultra) high vacuum. Utilizing rigidly mounted on-chip (instead of fiber supported) cavities will allow us to implement stable feedback cooling and to reach the chamber base pressure of 10^{-8} mBar (with mechanical losses $\gamma_m/2\pi$ in the MHz range) [15]. This will also improve the thermal anchoring of the cavity and therefore enable a higher intra-cavity photon number n_{cav} , which is now limited to $n_{cav} \sim 800$ because of thermo-optic heating. With a more careful design and fabrication, the cavity optical losses $\kappa/2\pi$ can be reduced to as low as 20 MHz in silicon [36] and 1 GHz in SiN [37]. Furthermore, optimization of the thickness of the structures can reduce the particle trapping distance to below 200 nm, resulting in an expected increase of the coupling rate by one order of magnitude (see SI and [25]). Incorporating all these improvements will allow to achieve $C_q > 10$ and thus place the system deep into the strong cooperativity regime. This will enable a new generation of chip-based levitated quantum sensors operating at room temperature. For example, the high bandwidth of our system ($\kappa \gg \Omega_m$) makes it an ideal platform for implementing quantum non-demolition measurements using pulsed interactions [38]. Exploiting the design capabilities for the spatial modes in photonic crystal cavities our system can also be used for studying effects of self-induced backaction and non-harmonic dynamics in both the classical and quantum regime [12]. Also, the expected force noise of 10^{-20} N/ $\sqrt{\text{Hz}}$ will allow a detailed study of short-range surface forces at sub-micron distances [7, 8].

Acknowledgements We thank Ramon Moghadas Nia for valuable lab support, Eugene Straver, Michael J. Burek and Marko Lončar for their technical advise on the tapered fibers, and Nikolai Kiesel and Lukas Novotny for helpful discussions. This project was supported by the European Research Council (ERC) CoG QLev4G and StG Strong-Q (Grant Agreements No 649008 and 676842), the Austrian Science Fund (FWF) under the projects F40 (SFB FOQUS), P28172, the Foundation for Fundamental Research on Matter (FOM) Projectruimte grant (15PR3210) and by the Netherlands Organisation for Scientific Research (NWO/OCW), as part of the Frontiers of Nanoscience program. L. M. is supported by the Vienna Doctoral School of Physics (VDS-P), R. R. is a recipient of a DOC fellowship of the Austrian Academy of Sciences at the University of Vienna and L. M., R. R., D. G. and U. D. are supported by the FWF under project W1210 (CoQuS).

[1] Wang, M. D., Yin, H., Landick, R., Gelles, J., and Block, S. M., Stretching DNA with optical tweezers. *Biophys J* 72(3), 1335–1346 (1997).

- [2] Jiao, J., Rebane, A. A., Ma, L., and Zhang, Y., Single-Molecule Protein Folding Experiments Using High-Precision Optical Tweezers. *Methods Mol Biol* **1486**, 357–390 (2017).
- [3] Bowman, R. W., Gibson, G. M., Padgett, M. J., Saglimbeni, F., and Di Leonardo, R., Optical Trapping at Gigapascal Pressures. *Phys. Rev. Lett.* **110**, 095902 (2013).
- [4] Li, T., Kheifets, S., Medellin, D., and Raizen, M. G., Measurement of the Instantaneous Velocity of a Brownian Particle. *Science* **328**(5986), 1673–1675 (2010).
- [5] Rondin, L. *et al.*, Direct measurement of Kramers turnover with a levitated nanoparticle. *Nature Nanotechnology* **12**, 1130 (2017).
- [6] Ricci, F. *et al.*, Optically levitated nanoparticle as a model system for stochastic bistable dynamics. *Nature Communications* **8**, 15141 (2017).
- [7] Ranjit, G., Cunningham, M., Casey, K., and Geraci, A. A., Zep-Newton force sensing with nanospheres in an optical lattice. *Phys. Rev. A* **93**, 053801 (2016).
- [8] Hempston, D. *et al.*, Force sensing with an optically levitated charged nanoparticle. *Applied Physics Letters* **111**(13), 133111 (2017).
- [9] Kaltenbaek, R. *et al.*, Macroscopic quantum resonators (MAQRO). *Experimental Astronomy* **34**(2), 123–164 (2012).
- [10] Moore, D. C., Rider, A. D., and Gratta, G., Search for Millicharged Particles Using Optically Levitated Microspheres. *Phys. Rev. Lett.* **113**, 251801 (2014).
- [11] Romero-Isart, O., Juan, M. L., Quidant, R., and Cirac, J. I., Toward quantum superposition of living organisms. *New Journal of Physics* **12**(3), 033015 (2010).
- [12] Neumeier, L., Quidant, R., and Chang, D. E., Self-induced back-action optical trapping in nanophotonic systems. *New Journal of Physics* **17**(12), 123008 (2015).
- [13] Kiesel, N. *et al.*, Cavity cooling of an optically levitated micron particle. *Proceedings of the National Academy of Sciences* **110**(35), 14180–14185 (2013).
- [14] Millen, J., Fonseca, P. Z. G., Mavrogordatos, T., Monteiro, T. S., and Barker, P. F., Cavity Cooling a Single Charged Levitated Nanosphere. *Phys. Rev. Lett.* **114**, 123602 (2015).
- [15] Jain, V. *et al.*, Direct Measurement of Photon Recoil from a Levitated Nanoparticle. *Phys. Rev. Lett.* **116**, 243601 (2016).
- [16] Asenbaum, P., Kuhn, S., Nimmrichter, S., Sezer, U., and Arndt, M., Cavity cooling of free silicon nanoparticles in high vacuum. *Nature Communications* **4**, 2743 (2013).
- [17] Kuhn, S. *et al.*, Nanoparticle detection in an open-access silicon microcavity. *Applied Physics Letters* **111**(25), 253107 (2017).
- [18] Li, T., Kheifets, S., and Raizen, M. G., Millikelvin cooling of an optically trapped microsphere in vacuum. *Nature Physics* **7**, 527 (2011).
- [19] Gieseler, J., Deutsch, B., Quidant, R., and Novotny, L., Subkelvin Parametric Feedback Cooling of a Laser-Trapped Nanoparticle. *Phys. Rev. Lett.* **109**, 103603 (2012).
- [20] Vovrosh, J. *et al.*, Parametric feedback cooling of levitated optomechanics in a parabolic mirror trap. *J. Opt. Soc. Am. B* **34**(7), 1421–1428 (2017).
- [21] Clerk, A. A., Girvin, S. M., and Stone, A. D., Quantum-limited measurement and information in mesoscopic detectors. *Phys. Rev. B* **67**, 165324 (2003).
- [22] Anetsberger, G. *et al.*, Near-field cavity optomechanics with nanomechanical oscillators. *Nature Physics* **5**, 909 (2009).
- [23] Chan, J. *et al.*, Laser cooling of a nanomechanical oscillator into its quantum ground state. *Nature* **478**, 89 (2011).
- [24] Burek, M. J. *et al.*, Fiber-Coupled Diamond Quantum Nanophotonic Interface. *Phys. Rev. Applied* **8**, 024026 (2017).
- [25] Thompson, J. D. *et al.*, Coupling a Single Trapped Atom to a Nanoscale Optical Cavity. *Science* **340**(6137), 1202–1205 (2013).
- [26] Goban, A. *et al.*, Superradiance for Atoms Trapped along a Photonic Crystal Waveguide. *Phys. Rev. Lett.* **115**, 063601 (2015).
- [27] Englund, D. *et al.*, Controlling the Spontaneous Emission Rate of Single Quantum Dots in a Two-Dimensional Photonic Crystal. *Phys. Rev. Lett.* **95**, 013904 (2005).
- [28] Hausmann, B. J. M. *et al.*, Coupling of NV Centers to Photonic Crystal Nanobeams in Diamond. *Nano Letters* **13**(12), 5791–5796 (2013).
- [29] Quan, Q. *et al.*, Single particle detection in CMOS compatible photonic crystal nanobeam cavities. *Opt. Express* **21**(26), 32225–32233 (2013).
- [30] Descharmes, N., Dharanipathy, U. P., Diao, Z., Tonin, M., and Houdré, R., Observation of Backaction and Self-Induced Trapping in a Planar Hollow Photonic Crystal Cavity. *Phys. Rev. Lett.* **110**, 123601 (2013).
- [31] Aspelmeyer, M., Kippenberg, T. J., and Marquardt, F., Cavity optomechanics. *Rev. Mod. Phys.* **86**, 1391–1452 (2014).
- [32] Diehl, R. *et al.*, Optical potential mapping with a levitated nanoparticle at sub-wavelength distances from a membrane. *arXiv:1803.04917 [physics.optics]* (2018).
- [33] Hryciw, A. C., Wu, M., Khanaliloo, B., and Barclay, P. E., Tuning of nanocavity optomechanical coupling using a near-field fiber probe. *Optica* **2**(5), 491–496 (2015).
- [34] Genes, C., Vitali, D., Tombesi, P., Gigan, S., and Aspelmeyer, M., Ground-state cooling of a micromechanical oscillator: Comparing cold damping and cavity-assisted cooling schemes. *Phys. Rev. A* **77**, 033804 (2008).
- [35] Wilson, D. J. *et al.*, Measurement-based control of a mechanical oscillator at its thermal decoherence rate. *Nature* **524**, 325 (2015).
- [36] Asano, T., Ochi, Y., Takahashi, Y., Kishimoto, K., and Noda, S., Photonic crystal nanocavity with a Q factor exceeding eleven million. *Opt. Express* **25**(3), 1769–1777 (2017).
- [37] Debnath, K. *et al.*, Ultrahigh-Q photonic crystal cavities in silicon rich nitride. *Opt. Express* **25**(22), 27334–27340 (2017).
- [38] Vanner, M. R. *et al.*, Pulsed quantum optomechanics. *Proceedings of the National Academy of Sciences* **108**(39), 16182–16187 (2011).
- [39] Frimmer, M. *et al.*, Controlling the net charge on a nanoparticle optically levitated in vacuum. *Phys. Rev. A* **95**, 061801 (2017).
- [40] We note that in our experiment, most particles are generated without residual charges. This contrasts other experimental reports where tens of positive charges are observed after trapping [39], and is subject to further investigation.

SUPPLEMENTARY INFORMATION

Cavity and fiber fabrication

Photonic crystal nanobeam patterns are exposed into a resist layer, on samples consisting of 350 nm films of LPCVD silicon nitride (SiN) deposited on Si substrates, using electron-beam lithography. We use a CHF_3/O_2 directional plasma etch to transfer arrays of nanobeam structures into the SiN film. The surface is thoroughly cleaned using a (4:1) piranha solution and the chip then dipped into diluted hydrofluoric acid (HF) to remove oxidation from the exposed silicon surfaces. The SiN devices are released from the substrate using a SF_6 plasma release. This method allows us to produce very clean and smooth surfaces with high yield. The nanobeams are designed to taper down into a thin bridge connecting it to the substrate (left side in Fig. S1a,b). This allows us to break the nanobeams off the substrate using a tapered fiber. These fibers are made by cleaving and stripping Corning SMF28 optical fibers and pulling them from a container of HF solution at a speed of $0.2 \mu\text{m/s}$ for 70 minutes using computer controlled motors. A small amount of o-xylene is used as a thin protective layer on the surface of the HF in order to prevent HF vapor from etching (and roughening) other parts of the fiber as it is pulled from the beaker [S1].

Transfer of the photonic crystal cavity to the tapered fiber

We image the tapered fiber clamped to its holder using an optical 50x microscope objective with a long working distance. The chip with arrays of the photonic crystal cavities is placed on a translational stage below the fiber. By controlling the chip position we can now move the fiber tip into contact with the tapered end of the photonic crystal cavity. Once a cavity with good resonance, coupling and optical Q is found, we break it off the chip by forcing the fiber against it. Optimization of the alignment is then carried out with the help of a tungsten tip placed perpendicular to the fiber on a separate stage. Due to the HF tapering the fiber surface is quite rough [S1] and in order to increase the contact surface to the cavity and improve the connection strength, we dip the tapered fiber into UV glue and cure it before picking up the device. This results in a strong bond which does not affect the coupling efficiency and greatly reduces the chances to lose one of the photonic crystal cavities while transferring it into the vacuum chamber.

Particle loading

We load the nanoparticles into the tweezer trap at room pressure, keeping the cavity in vacuum in a separate chamber connected to the main chamber through a load lock valve. Once the particle is trapped and the main chamber is evacuated to around 1 mbar, we move the cavity positioner onto its holder

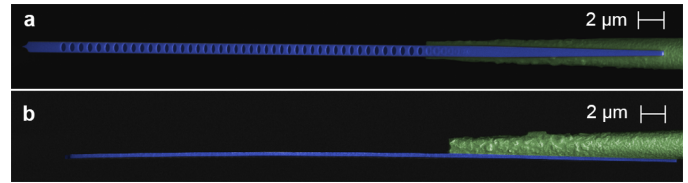


FIG. S1: **Photonic crystal cavity.** Top (a) and side (b) SEM image of the photonic crystal cavity (blue) and tapered fiber (green) used for the measurements presented in the main text. The roughness of the HF tapered fiber is mitigated by UV glue, which improves the contact to the cavity and a stronger van der Waals bond.

in proximity to the trapping objective. Imaging through the trapping objective allows us to precisely control its position. Using a dichroic mirror we can separate the trapping laser from the green ($\lambda_{im} = 532 \text{ nm}$) illumination light which is used to image the particle and the cavity at the same time. In order to obtain a well aligned trapping beam during the experiment, we tilt the last mirror, thereby moving the particle above the center of the objective field of view and center the cavity by controlling its nanopositioner (Fig. S2). Once the cavity is in place,

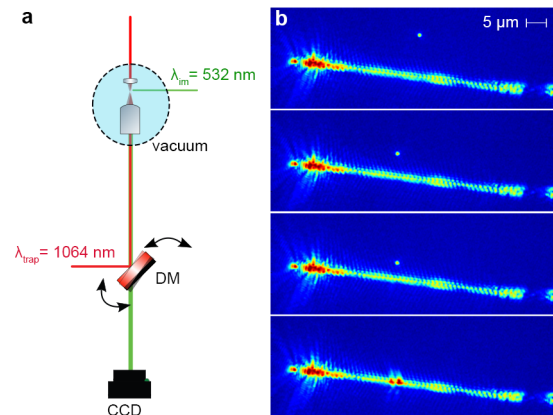


FIG. S2: **Position control of the levitated nanoparticle.** a, Position control of the trapped particle is achieved by tilting of the dichroic mirror (DM) just before the objective. As also shown by Diehl *et al.* [S2], the trapping objective is also used to image the particle and photonic crystal cavity by collection of scattered $\lambda_{im} = 532 \text{ nm}$ light coming from the side. b, Scattering images of the nanoparticle approaching the photonic crystal cavity as the trapping beam is tilted. When the particle is in front of the cavity, not perfect extinction of the reflected trapping light causes the camera to saturate hiding the particle.

we move the trapped particle in front of the cavity by tilting the mirror back into its original position. The cavity output signal allows us to measure the coupling strength and particle frequency, determining the particle position inside the lattice: if the particle is measured to be in the second or third lobe away from the cavity, we tilt the mirror away again, move the cavity closer into the microscope's focus and repeat the proce-

ture until we observe large optomechanical coupling (Fig. 4 in the main text). After the particle is positioned in the first lobe, we define the lateral positioning in the cavity field, by moving the cavity itself in steps of ~ 10 nm.

Detection efficiency and sensitivity

We pump the cavity with 260 nW, and the output field is guided to homodyne detection. The total detection efficiency is $\eta = \eta_{loss}\eta_q\kappa_{in}/\kappa = 0.09$, with $\kappa_{in}/\kappa = 0.5$ the ratio of cavity input to total energy decay rate, $\eta_{loss} = 0.22$ the transmission of all other optical components, and $\eta_q = 0.85$ the detector quantum efficiency at $\lambda = 1550$ nm. In contrast, for far-field detection, the trapping beam is recollimated by a secondary objective together with the particle's scattered light and directed to a balanced detector where the common laser noise is cancelled. It is attenuated to typically 1 mW in order to stay in the linear regime of the photodetector. In this case the detection efficiency of the particle scattered light is estimated to be below $\eta_F \sim 10^{-3}$ [S3]. For both detection schemes we measure comparable signal-to-noise ratio (SNR), where $\sqrt{\text{SNR}} \propto \sqrt{\dot{n}_{det}\chi}$, \dot{n}_{det} the rate of detected photons and χ the single photon measurement strength (Fig. S3). This defini-

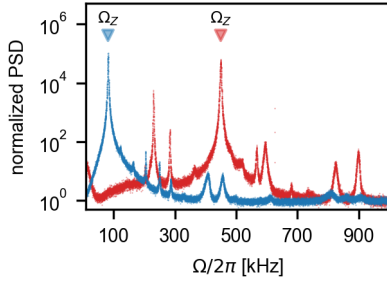


FIG. S3: **Far field and cavity detection.** Comparison between the far field detection (blue) and the cavity near field detection (red) power spectral densities. The power detected in the far field case is of about 1 mW, while in the case of cavity detection, the signal reaching the homodyne detection is of less than 60 nW. The significant difference in mechanical frequencies is due to the formation of a standing wave trap in presence device.

tion gives us an estimate of the ratio of single photon measurement strengths for the two detection schemes of $\chi_0/\chi_F \sim 10^2$ with χ_0 and χ_F the near and far field single photon sensitivities respectively. In addition, while the single photon measurement strength for our experimental parameters $\chi_0 = 2g_0/\kappa = 5.2 \times 10^{-6}$ shows room for improvement, it

is already very close to the ideal, lossless, free space strength given by $\chi_F^{max} = 4\pi x_{ZPF}/\lambda_{trap} = 2.0 \times 10^{-5}$ [S4], which is fundamentally limited. Detection efficiency can also be significantly improved with minimal effort by reduction of optical losses $\eta_{loss} = \eta_{cav}\eta_{path}$. Currently η_{path} includes the loss of many fiber connectors, which can be replaced by almost lossless splices. At the same time, while all measurements were performed with a waveguide-fiber coupling efficiency of $\eta_{cav} = 0.32$, with a more careful alignment we have measured a single pass coupling efficiency of $\eta_{cav} = 0.96$ as previously shown by Burek *et al.* [S1].

Calibration of the optomechanical coupling

The calibration of the frequency shift per displacement $G = \frac{d\omega_{cav}}{dx}$ was carried out by evaluating the measured power spectral densities $S_W(\Omega)$ compared to the measured shot-noise level S_W^{sn} . Using the known Poissonian statistics governing the photon shot-noise, one can estimate the amount of detected photons and their contribution to the noise level. This allows to calibrate the signal in units of photons. The position spectral density of the particle is that of a damped harmonic oscillator subject to a stochastic Langevin force

$$S_{xx}(\Omega) = 2 \langle x^2 \rangle \frac{\gamma \Omega_m^2}{(\Omega_m^2 - \Omega^2)^2 + \gamma^2 \Omega^2}, \quad (\text{S1})$$

where the particle is in thermal equilibrium with its bath $\langle x^2 \rangle = \frac{k_B T}{m \Omega_m^2}$. The fluctuations of the cavity resonance are related to the particles position through $G = \frac{d\omega_{cav}}{dx}$

$$S_{\omega\omega}(\Omega) = G^2 S_{xx}(\Omega). \quad (\text{S2})$$

Considering the optical annihilation operator \hat{a} , it is convenient to make use of the input-output formalism in order to evaluate the mechanically induced noise [S5]. The cavity field reads

$$\hat{a} = \frac{\sqrt{\kappa_{in}}\hat{a}_{in} + \sqrt{\kappa_0}\hat{a}_0}{-i\Delta + \frac{\kappa}{2}}, \quad (\text{S3})$$

where κ_0 is the intrinsic cavity decay rate, $\Delta = \omega_L - \omega_{cav} + \delta\omega$ the detuning between the laser frequency ω_L and the cavity resonance ω_{cav} , $\delta\omega$ the mechanical induced frequency fluctuations, \hat{a}_0 and \hat{a}_{in} the annihilation operators defining the environment vacuum and input field amplitudes respectively. The output field \hat{a}_{out} is given by

$$\hat{a}_{out} = \hat{a}_{in} - \sqrt{\kappa_{in}}\hat{a} = \hat{a}_{in} - \sqrt{\kappa_{in}} \left[\sqrt{\kappa_{in}}\hat{a}_{in} + \sqrt{\kappa_0}\hat{a}_0 \right] \left[\frac{\kappa/2}{\Delta^2 + \left(\frac{\kappa}{2}\right)^2} + i \frac{\Delta}{\Delta^2 + \left(\frac{\kappa}{2}\right)^2} \right] \sim -i \frac{2\delta\omega}{\kappa} \hat{a}_{in} - i \frac{2\delta\omega}{\kappa} \hat{a}_0 - \hat{a}_0, \quad (\text{S4})$$

where the approximation arises when considering a resonant laser drive $\omega_L = \omega_{cav}$, and mechanical resonance fluctuations that are much smaller than the cavity linewidth $\Delta = \delta\omega \ll \kappa$. In addition, critical coupling $\kappa/2 = \kappa_{in} = \kappa_0$ allows us to further reduce the parameter space. Using eq. (S4), considering a

strong coherent input field $\hat{a}_{in} \rightarrow \hat{a}_{in} + \alpha_{in}$ with α_{in} real valued, the commutation relation $[\hat{a}(t), \hat{a}^\dagger(t + \tau)] = \delta(\tau)$, and defining the phase quadrature operator as $\hat{Y} = \frac{\hat{a}_{out} - \hat{a}_{out}^\dagger}{\sqrt{2i}}$, the phase quadrature spectral density can be computed:

$$S_{YY}(\Omega) = \int_{-\infty}^{+\infty} d\tau e^{i\Omega\tau} \langle \hat{Y}(t + \tau) \hat{Y}(t) \rangle \sim 2 \frac{4\bar{\alpha}_{in}^2}{\kappa^2} \int_{-\infty}^{+\infty} d\tau e^{i\Omega\tau} \langle \delta\omega(t + \tau) \delta\omega(t) \rangle + \frac{1}{2} \int_{-\infty}^{+\infty} d\tau e^{i\Omega\tau} \delta(\tau) \quad (S5)$$

$$= 2 \frac{4\bar{\alpha}_{in}^2}{\kappa^2} S_{\omega\omega}(\Omega) + \frac{1}{2} = 2\bar{\alpha}_{in}^2 S_{\varphi\varphi}(\Omega) + \frac{1}{2},$$

The output signal is then attenuated by optical losses η_{loss} , and amplified by a strong local oscillator of amplitude β_0 in a homodyne detection scheme. In addition, we consider the non unity quantum efficiency of the detectors yet as another attenuation channel η_q , affecting the expectation values of the field operator products ($\alpha_{in} \rightarrow \sqrt{\eta_{loss}} \sqrt{\eta_q} \alpha_{in}$, $\beta_0 \rightarrow \sqrt{\eta_q} \beta_0$) [S6]. At each detector the optical power spectral density is

$$S_{PP}(\Omega) = 4\eta_{loss}\eta_q^2 h^2 \nu^2 \bar{\alpha}_{in}^2 \beta_0^2 S_{\varphi\varphi}(\Omega) + S_{PP}^{sn}, \quad (S6)$$

where $S_{PP}^{sn} = h^2 \nu^2 \eta_q \beta_0^2$ is the two sided photon shot noise level. When a photon is detected, it is converted into an electron current: $i(t) = n(t)e$, where $n(t)$ is the number of detected photons and e the electron charge. Non unity of the quantum efficiency of detectors has been already considered in eq. (S6) as an effective optical loss [S6]. Photocurrents from each detector are subtracted and the DC component as well as classical laser noise are cancelled. The current can then be amplified and converted into a voltage signal via the transimpedance amplifier $v(t) = g_t i_{AC}(t)$. It is now convenient to define the lossless optical power to voltage conversion factor as

$$G_{RF} = \frac{g_t e}{h\nu}. \quad (S7)$$

Finally, the measured two sided power spectral density reads:

$$S_W(\Omega) = \frac{G_{RF}^2}{R_L} 4S_{PP}(\Omega) = \frac{G_{RF}^2}{R_L} 4\eta_q^2 \eta_{loss} P_{in} P_{LO} \frac{4G^2}{\kappa^2} S_{xx}(\Omega) + S_W^{sn}, \quad (S8)$$

where $P_{in} = h^2 \nu^2 \bar{\alpha}_{in}^2$ ($P_{LO} = h^2 \nu^2 \beta_0^2$) is the cavity input (local oscillator) power, R_L is the input impedance of the measuring instrument and $S_W^{sn} = G_{RF}^2 \eta_q P_{LO} h\nu / R_L$ the two sided shot noise level in units of W/Hz [S11]. The conversion factor G_{RF} can now be written in terms of measured quantities:

$$G_{RF} = \sqrt{\frac{S_W^{sn} R_L}{\eta_q P_{LO} h\nu}}. \quad (S9)$$

Substituting Eq. (S9) into (S8), we obtain

$$S_W(\Omega) = \frac{S_W^{sn} \eta_q}{h\nu} 4\eta_{loss} P_{in} \frac{4G^2}{\kappa^2} S_{xx}(\Omega) + S_W^{sn}. \quad (S10)$$

The optomechanical coupling can now be derived by integrating the power spectral density

$$G = \sqrt{\frac{\int_{-\infty}^{+\infty} S_W(\Omega) \frac{d\Omega}{2\pi}}{\frac{k_B T}{m\Omega^2}} \frac{\kappa^2 h\nu}{S_W^{sn} 8\eta_{loss} \eta_q P_{in}}}. \quad (S11)$$

In Eq. (S11) the negative contribution arising from the shot-noise is neglected as it is orders of magnitude lower due to the large optomechanical coupling rate.

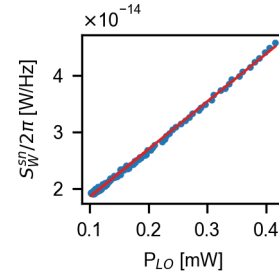


FIG. S4: **Shot-noise power dependence.** Linear dependence of the shot-noise level as a function of optical power of the local oscillator.

Cavity heating

The cavity resonance is also strongly dependent on heating, arising both from the optical field of the tweezer and the cavity power itself. Heating effects are particularly evident in vacuum, where heat dissipation is less efficient. While the tweezer incident power only induces a constant frequency shift, which is different for each position of the cavity, heating arising from the cavity pump field strongly depends on

the wavelength which defines the cavity population, leading to a thermo-optic instability (Fig. S5). During the measurements, at each position of the cavity with respect to the tweezer light, induced heating varies shifting the cavity resonance. We therefore scan the cavity at each step and set the laser on resonance, ensuring optimal optomechanical response (Fig. S5). As for the internal heating, effects are visible when scanning the pump wavelength: the expected Lorentzian response in the reflected signal shows an asymmetry due to dynamic heating effects when the power is too high. We run the experiments with $P_{in} \sim 260$ nW ($n_{cav} \sim 800$), far below the input powers where a sizable deviation from the Lorentzian line shape can be observed.

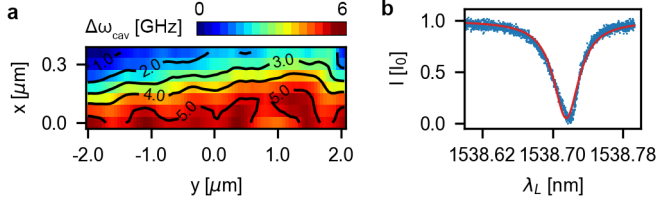


FIG. S5: **Static and dynamic cavity heating.** **a**, Cavity heating induced by the trapping field at different positions: the resonance is shifted by up to 5 GHz, while the cavity response function remains unaffected. This map was taken during the scan in Fig. 2b in the main text. **b**, Cavity heating induced by the intra-cavity field causes an asymmetry in the cavity response function. Above a certain threshold, the pump will cause dynamic instability of the cavity.

Trapping distance simulation

As shown by Thompson *et al.* [S8], the lattice formation, particularly the trapping locations with respect to the photonic crystal's surface are defined by the thickness of the slab L :

$$z_i = -\frac{\phi}{4\pi} \lambda_{trap} + n \frac{\lambda_{trap}}{2}, \quad i = 0, 1, 2, \dots \quad (\text{S12})$$

with

$$\phi = \tan^{-1} \left(\frac{2n \cos(nkL)}{(1+n^2) \sin(nkL)} \right) \quad (\text{S13})$$

where $k = 2\pi/\lambda_{trap}$ is the optical wavevector and n the refractive index in silicon nitride. The SEM measured thickness of our photonic crystal cavity is 310 nm, corresponding to $z_0 \sim 380$ nm. With a particle size of $r \sim 70$ nm the surface to surface distance is $d_0 = z_0 - r \sim 310$ nm. Fig. (S7) shows how, by reducing the cavity thickness to about 200 nm, the trapping position can be reduced to $z_0 \sim 220$ nm, corresponding to a surface to surface distance of $d_0 \sim 150$ nm.

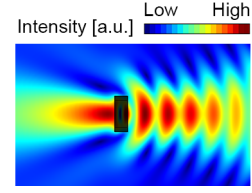


FIG. S6: **Optical lattice.** FEM simulation of the trap formation from the reflection of the tweezer light focused from the left on to the photonic crystal cavity (dark shaded area).

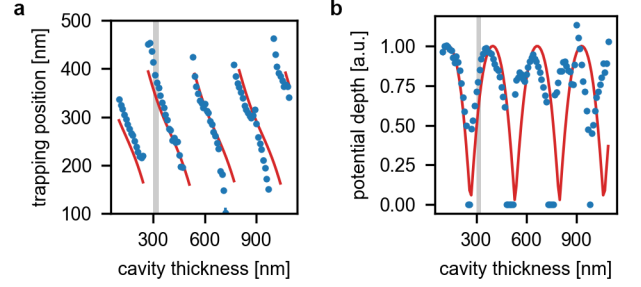


FIG. S7: **Trap position simulation.** **a**, FEM simulation of the trapping position z_0 as a function of the cavity thickness. **b**, Potential depth simulation as a function of the cavity thickness. Red solid lines show the theoretical expected value considering a plane incident wave. Gray shaded areas indicate our experimental conditions: thickness of 310nm, measured by SEM imaging.

Cavity field simulation

The design of the photonic crystal cavity was based on finite element simulation. This allows us to predict the amount of evanescent field and optimize coupling. For a qualitative understanding of the coupling and fitting of the data, we use a simple model of the cavity field which does not account for the details of the photonic structure, only the dominant mode shape. This model considers a standing wave with an intensity oscillation period of $\lambda/2$, Gaussian mode confinement in all directions inside the material and exponential evanescent field decay outside. Polarization and surface scattering are not considered. Close to the cavity axis (blue line in Fig. S8c) simulation agrees well with our model, however as one moves away from the center of the cavity, surface effects give rise to a more complex x dependence, reducing the contrast of the field oscillations as shown in FEM simulation (Fig. S8). This effect results in non-vanishing coupling to the z mode as soon as the particle is off the cavity axis.

$$E^* E = E_0^2 e^{-\frac{y^2}{2\sigma_y}} e^{-\frac{x^2}{2\sigma_x}} e^{-\beta\sqrt{x^2+z^2}} \sin^2 \left(\frac{2\pi}{\lambda} y \right) \quad (\text{S14})$$

$$g_0^z(y) \propto \partial_z E^* E \propto \left| 1 - \cos \left(2 \frac{2\pi}{\lambda} y \right) \right| \quad (\text{S15})$$

$$g_0^y(y) \propto \partial_y E^* E \propto \left| \sin \left(2 \frac{2\pi}{\lambda} y \right) \right| \quad (\text{S16})$$

$$g_0^x(y) \propto \partial_x E^* E \propto \left| 1 - \cos\left(2\frac{2\pi}{\lambda}y\right) \right| \quad (\text{S17})$$

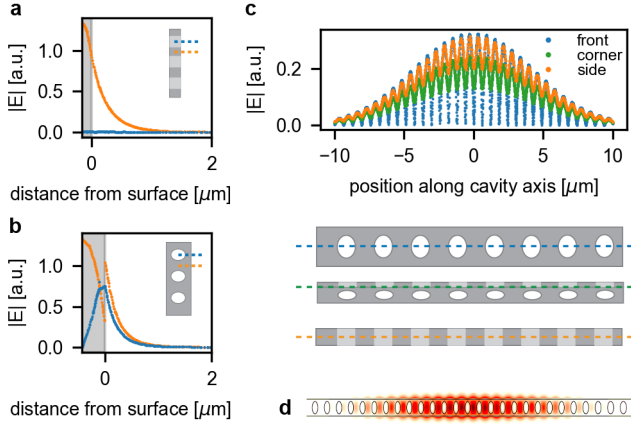


FIG. S8: **FEM simulation of the cavity field.** **a**, Depicted is the cavity field as a function of distance from the cavity surface moving away from its wide side, in correspondence of a hole (blue) or of the matter region (orange). The shaded area indicates the cavity extension. **b**, Cavity field simulation as a function of distance from its narrow side in correspondence of a hole (blue) or matter (orange). **c**, Simulation of the evanescent cavity field evaluated at 250 nm distance from the surface, and in front of the cavity (blue), at a corner (green) and at the side of the cavity (orange). Whenever one moves away from the cavity axis the contrast of the oscillation is reduced and the field never vanishes. **d**, heat map of the simulated cavity field intensity.

Optomechanical coupling simulation

A study of the expected coupling was carried out by FEM simulation in a static fashion. The expected cavity resonances were evaluated by placing a 75 nm radius nanoparticle at defined distance from the cavity surface. Simulations have been run at different distances both on the side and in front of the cavity. Simulation was fitted to exponential decay of the cavity field. Assuming small particle displacements optomechanical coupling can be estimated in the linearized case:

$$G = \left. \frac{\partial \omega_{cav}}{\partial z} \right|_{z=d} + \mathcal{O}(\delta \omega_{cav}^2) \quad (\text{S18})$$

At a distance of $d = z_0 - r \sim 310$ nm the expected coupling and frequency shift per displacement of 11 and 7 MHz/nm for the case of particle in front and on the side of the cavity respectively (Fig. S9). The lower measured values can be easily explained by the fact that measurements were made slightly off the cavity axis as discussed previously. The measured power spectral densities also show peaks at twice the mechanical frequency. These are the result of two distinct effects: nonlinear potential [S9] and quadratic coupling [S10]. While potential nonlinearities result into a constant relative contribution of the

harmonic peak, nonlinear optomechanical couplings depend on the field at the given position.

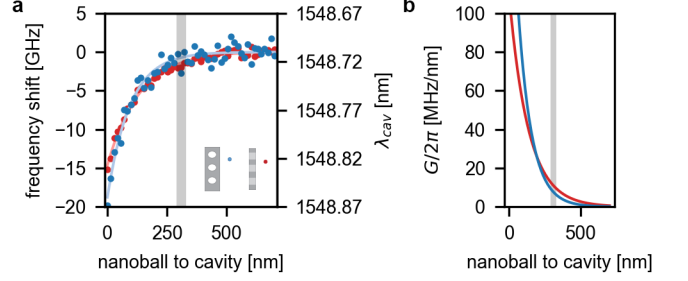


FIG. S9: **Optomechanical frequency shift simulation.** **a**, FEM simulation of cavity frequency shift as function of the particle surface to cavity surface distance. The plot shows both simulation for the case of the particle in front (red) and on the side (blue) of the cavity. Gray shaded area indicates our experimental conditions: trapping at $z_0 \sim 380$ nm results in surface to surface distance of $d_0 \sim 310$ nm. Exponential decay follows the evanescent field amplitude. **b**, Estimated frequency shift per displacement as a function of d .

- [S1] Burek, M. J. *et al.*, Fiber-Coupled Diamond Quantum Nanophotonic Interface. *Phys. Rev. Applied* **8**, 024026 (2017).
- [S2] Diehl, R. *et al.*, Optical potential mapping with a levitated nanoparticle at sub-wavelength distances from a membrane. *arXiv:1803.04917 [physics.optics]* (2018).
- [S3] Jain, V. *et al.*, Direct Measurement of Photon Recoil from a Levitated Nanoparticle. *Phys. Rev. Lett.* **116**, 243601 (2016).
- [S4] Vanner, M. R., Hofer, J., Cole, G. D., and Aspelmeyer, M., Cooling-by-measurement and mechanical state tomography via pulsed optomechanics. *Nature Communications* **4**, 2295 EP – (2013).
- [S5] Aspelmeyer, M., Kippenberg, T. J., and Marquardt, F., Cavity optomechanics. *Rev. Mod. Phys.* **86**, 1391–1452 (2014).
- [S6] Paul, H., Shot Noise in Photodetectors and Vacuum Fluctuations. *Journal of Modern Optics* **35**(7), 1225–1235 (1988).
- [S7] Bavor, H. A. and Ralph, T. C., *A Guide to Experiments in Quantum Optics*, (Wiley-vch, Weinheim2004).
- [S8] Thompson, J. D. *et al.*, Coupling a Single Trapped Atom to a Nanoscale Optical Cavity. *Science* **340**(6137), 1202–1205 (2013).
- [S9] Gieseler, J., Novotny, L., and Quidant, R., Thermal nonlinearities in a nanomechanical oscillator. *Nature Physics* **9**, 806 (2013).
- [S10] Thompson, J. D. *et al.*, Strong dispersive coupling of a high-finesse cavity to a micromechanical membrane. *Nature* **452**, 72 (2008).
- [S11] Alternatively the photon shot-noise level can be derived by considering the Poissonian photon statistics of coherent fields ($\Delta n^2 = \bar{n}$). The photo-current noise is then $\Delta i^2 = 2i e B W = \frac{2P e^2 \eta_q B W}{h\nu}$, and $\Delta v^2 = \frac{2g_L^2 P e^2 \eta_q B W}{h\nu}$ [S7]. The one sided shot-noise power spectral density is $\bar{S}_W^{sn} = \frac{\Delta v^2}{R_L B W} = \frac{2g_L^2 P e^2 \eta_q}{R_L h\nu} = \frac{2G_{RF}^2 \eta_q P h\nu}{R_L} = 2S_W^{sn}$, where the total power reaching the detector is $P = P_{LO} + \eta_{loss} P_{in} \sim P_{LO}$.